



## Strathprints Institutional Repository

**Sharma, A. S. and Eliasson, B. and Milikh, G. M. and Najmi, A. and Papadopoulos, K. and Shao, X. and Vartanyan, A. (2016) Low-frequency waves in HF heating of the ionosphere. In: Low-Frequency Waves in Space Plasmas. Geophysical Monograph Series, 216 (1). American Geophysical Union, Hoboken, New Jersey, USA, pp. 31-49. ISBN 978-1-119-05495-5 , <http://dx.doi.org/10.1002/9781119055006.ch3>**

This version is available at <http://strathprints.strath.ac.uk/57288/>

**Strathprints** is designed to allow users to access the research output of the University of Strathclyde. Unless otherwise explicitly stated on the manuscript, Copyright © and Moral Rights for the papers on this site are retained by the individual authors and/or other copyright owners. Please check the manuscript for details of any other licences that may have been applied. You may not engage in further distribution of the material for any profitmaking activities or any commercial gain. You may freely distribute both the url (<http://strathprints.strath.ac.uk/>) and the content of this paper for research or private study, educational, or not-for-profit purposes without prior permission or charge.

Any correspondence concerning this service should be sent to Strathprints administrator: [strathprints@strath.ac.uk](mailto:strathprints@strath.ac.uk)

# 3

## Low-Frequency Waves in HF Heating of the Ionosphere

A. S. Sharma,<sup>1</sup> B. Eliasson,<sup>1,2</sup> G. M. Milikh,<sup>1</sup> A. Najmi,<sup>1</sup> K. Papadopoulos,<sup>1</sup>  
X. Shao,<sup>1</sup> and A. Vartanyan<sup>1</sup>

### 3.1. INTRODUCTION

Ionospheric heating experiments have enabled an exploration of the ionosphere as a large-scale natural laboratory for the study of many plasma processes. These experiments inject high-frequency (HF) radio waves using high-power transmitters and an array of ground- and space-based diagnostics. The heating of the plasma has led to many new phenomena such as modulation of the ionospheric current system and generation of low-frequency electromagnetic radiation [Papadopoulos *et al.*, 1989; 2011a, b; Stubbe, 1996], stimulated emissions [Leyser, 2001], plasma waves and turbulence [Guzdar *et al.*, 2000], small-scale irregularities or striations [Mishin *et al.*, 2004], and pump-induced optical processes [Bernhardt *et al.*, 1989; Pedersen *et al.*, 2009]. Among the ionospheric heating facilities worldwide, the High Frequency Active Auroral Research Program (HAARP) located at Gakona, Alaska, has the highest power HF transmitter and a comprehensive set of diagnostics. The transmitter array of 180 crossed dipoles that are arranged in a 12 by 15 rectangular grid are phased together to produce up to 3.6 MW of radiated power in a band from 2.8 to 10 MHz. The HF heating experiments conducted using HAARP facility has generated low-frequency waves [Papadopoulos *et al.*, 2011a, b] in all the three ranges, namely ultra low frequency (ULF, <10 Hz), extremely low frequency (ELF, 0.3–3 kHz), and very low frequency (VLF, 3–30 kHz).

The low-frequency waves generated in the ionosphere during heating experiments with modulated HF waves (1–10 MHz) originate from multiple physical mechanisms that operate at different altitudes and conditions. A mechanism that is already demonstrated is the modulation of the D/E region conductivity by modulated HF heating, and this requires the presence of an electrojet current, namely the auroral electrojet. The associated modification of the electrojet current creates an effective antenna radiating at the modulation frequency [Stubbe *et al.*, 1981; Papadopoulos *et al.*, 1989; Stubbe, 1996]. This mechanism of low-frequency wave generation by a modulated heating of the auroral electrojet, at ~80 km altitude in the D/E region, is referred to as the polar electrojet (PEJ) antenna. In another mechanism, modulated HF waves heat the plasma in the F region, producing a local hot spot and thus a region of strong gradient in the plasma pressure. This induces a diamagnetic current on the time scale of the modulation frequency, which excites the hydromagnetic waves. In this mechanism, there is no quasi-steady or background current, and the wave excitation is controlled, for example, by the plasma conditions, HF modulation frequency, and size of the heated region. This is the mechanism that has been studied in simulations of the high-latitude ionosphere [Papadopoulos *et al.*, 2011a; Eliasson *et al.*, 2012] for conditions typically corresponding to the HAARP facility. Experiments at HAARP have verified this mechanism and provided details of the key features [Papadopoulos *et al.*, 2011b]. Another mechanism for generating low-frequency waves in the ELF range was motivated by observations from the DEMETER satellite during experiments at HAARP with no modulation of the HF power. These waves have been identified as

<sup>1</sup>Department of Astronomy, University of Maryland, College Park, Maryland, USA

<sup>2</sup>SUPA, Physics Department, University of Strathclyde, Glasgow, Scotland, UK

whistlers with frequencies close to that of lower hybrid waves and generated by parametric processes [Vartanyan *et al.*, 2016]. The mid-latitude ionosphere has no steady large-scale current or electrojet, and modulated HF heating is expected to generate low-frequency waves due to the processes similar to those of the high-latitude ionosphere. Numerical simulations of the modulated heating in the mid-latitude ionosphere show that the geometry of Earth's dipole field plays an important role in their propagation to the magnetosphere [Sharma *et al.*, 2016]. The excitation and propagation of low-frequency waves in HF heating of the ionosphere is presented in this chapter. The theoretical aspects and the associated models and simulations, and the results from experiments, mostly from the HAARP facility, are presented together to provide a comprehensive interpretation of the relevant plasma processes. The chapter is organized as follows. Section 3.2 presents the plasma model of the ionosphere for describing the physical processes during HF heating, the numerical code, and the simulations of the excitation of low-frequency waves by HF heating. The simulations of the high- and mid-latitude ionosphere are presented in Sections 3.3 and 3.4, respectively. The role of kinetic processes associated with wave generation is briefly discussed in Section 3.5, and the main conclusions of the chapter are presented in Section 3.6.

### 3.2. MODELING LOW-FREQUENCY WAVES IN HF HEATING

The hydromagnetic waves in the ionosphere can be described, in general, by the MHD model, in which all plasma species are magnetized. The main characteristics of the ionospheric plasma are shown in Figure 3.1. The ionosphere has a density maximum and the corresponding Alfvén speed minimum at an altitude of  $\sim 300$  km. At high-latitude conditions, the geomagnetic field is directed vertically downward. In the E region altitudes of 80 to 120 km, where the ion-neutral collision frequency  $\nu_{in}$  is larger than the ion cyclotron frequency  $\omega_{ci}$ , the ions are strongly coupled to the neutrals, and the Hall conductivity dominates the dynamics. The dominant low-frequency mode is the helicon mode [Greifinger, 1972; Papadopoulos *et al.*, 1994; Zhou *et al.*, 1996], which is the low-frequency ( $\omega \ll \omega_{ci}$ ) branch of the whistler wave, and it is carried by the electrons, since the ions are essentially immobile due to their strong coupling to the neutrals. In this region, the Hall conductivity  $\sigma_H$  dominates the Pedersen conductivity  $\sigma_P$ . This altitude dependence of the conductivities has important consequences in the propagation of waves, namely mode conversion between magnetosonic and shear Alfvén waves [Hughes, 1983].

The propagation of low-frequency waves ( $\omega \ll \omega_{ci} \ll \omega_{ce}$ ) in the ionosphere is described by using a collisional

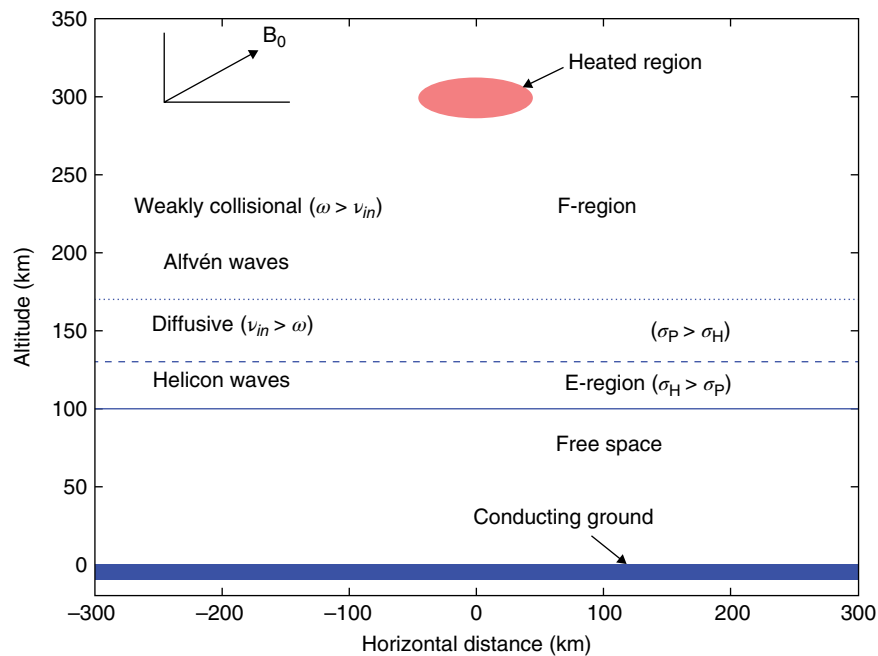


**Figure 3.1** Sketch of the ionosphere (above  $z = 100$  km, with free space below and a conducting ground) and the regions characterized by the relative magnitudes of the Hall ( $\sigma_H$ ) and Pederson ( $\sigma_P$ ) conductivities. The space-dependent geomagnetic field  $B_0$  magnetizes the plasma. The heated region is located in the F region at an altitude of 300 km. From Eliasson *et al.* [2012].

Hall–MHD model of the plasma. Neglecting the electron inertia, we can write the momentum equation governing the electron flow velocity  $\mathbf{v}_e$  in the electric field  $\mathbf{E}$  and magnetic fields  $\mathbf{B}$  as

$$\mathbf{0} = -\frac{e}{m_e}(\mathbf{E} - \mathbf{v}_e \times \mathbf{B}_0) - \nu_{en} \mathbf{v}_e - \frac{\nabla P_e}{n_0} \quad (3.1)$$

where  $P_e(\mathbf{r}, t) = n_0 T_e(\mathbf{r}, t)$  represents the modulated electron pressure due to local heating,  $n$  is the electron density,  $T_e(\mathbf{r}, t)$  is the electron temperature in energy units,  $\nu_{en}(\mathbf{r})$  is the electron-neutral collision frequency,  $e$  is the magnitude of the electron charge, and  $m_e$  is the electron mass.

The ion fluid velocity  $\mathbf{v}_i$  is governed by the ion momentum equation

$$\frac{\partial \mathbf{v}_i}{\partial t} = \frac{e}{m_i}(\mathbf{E} - \mathbf{v}_i \times \mathbf{B}_0) - \nu_{in} \mathbf{v}_i \quad (3.2)$$

where  $\nu_{in}$  is the ion-neutral collision frequency and  $m_i$  is the ion mass. The electric and magnetic fields are governed by Faraday's and Ampère's laws

$$\nabla \times \mathbf{E} = -\frac{\partial \mathbf{B}}{\partial t} \quad (3.3)$$

and

$$\nabla \times \mathbf{B} = \mu_0 e n_0(\mathbf{r})(\mathbf{v}_i - \mathbf{v}_e) \quad (3.4)$$

where  $\mu_0$  is the magnetic permeability in vacuum. The plasma is considered quasi-neutral with equal electron and ion number densities.

The heating of the ionosphere by HF waves from ground transmitters involves many physical processes with a wide range of space and time scales. On the shortest scales, the large-amplitude HF waves act as pump waves for wave–wave coupling and stimulated processes. The stimulated electromagnetic emissions (SEE) have frequencies around the pump wave and have been studied extensively through theory, numerical simulations, and experiments [Leyser, 2001]. The pump wave frequency is typically a few MHz and near the electron plasma frequency in the pump wave–plasma interaction region and the SEE covers a typical spectral width of roughly  $\pm 100$  kHz. The nonlinear interaction among the wave modes with the pump wave also leads to secondary electromagnetic radiation in the VLF, ELF, and ULF bands at much lower frequencies [Barr, 1998]. A pump wave excited process at the highest frequencies leads to

emissions at optical frequencies, observed in HF pump-enhanced airglow [Bernhardt *et al.*, 1989].

On longer space and time scales, the HF pump drives processes through the ponderomotive and thermal nonlinearities [Gurevich, 2007] and results in phenomena such as self-focusing instabilities. Early observations of the effects of HF waves showed self-focusing of electromagnetic waves in the ionosphere, and these are attributed to the thermal self-focusing instability [Guzdar *et al.*, 2000]. The structuring of the ionospheric plasma into field-aligned striations is one of the important phenomena in HF heating experiments, with the transverse size ranging from less than 1 m to more than 1 km and field-aligned length of  $\sim 10$  km.

The plasma physics of HF heating thus involves a multitude of processes, including the pumping of high-frequency upper-hybrid and plasma waves and the resulting turbulence, and trapping in the striations. The striations themselves get bunched together, generating larger scale structures. In these interactions the electrons gain energy, through the formation of high-energy tails and subsequent thermalization [Mishin *et al.*, 2004]. On the scales relevant to the low-frequency waves, the various processes due to the HF waves result in a local region with enhanced temperature, and the size and duration of HF heating are determined by the beam size and modulation frequency, respectively. The processes at such the short scales do not play a direct role in this study. In the volume-averaged picture we use, the heated region is modeled as a region of enhanced electron pressure  $P_e$ . In our numerical model, the electron temperature is assumed to have a Gaussian profile and with azimuthal symmetry:

$$T_e = T_{mod} \tanh^2\left(\frac{t}{D_t}\right) \cos(\omega t) \exp\left[-\frac{r_\theta^2}{L_r^2} - \frac{(z - z_o)^2}{L_z^2}\right] \quad (3.5)$$

where  $T_{mod}$  is the modulation amplitude of the electron temperature,  $D_t$  is the rise time,  $L_r$  is the width in the plane at  $z = z_o$ ,  $L_z$  is the vertical width of the heated region, and the heating is modulated at frequency  $\omega$ . As in Eliasson *et al.* [2012], the slow mean temperature increase due to the HF heating is neglected because it does not contribute significantly to the wave dynamics. The actual form of the heated region, as well as the background magnetic field changes with the latitude of the heated region, are discussed in the following sections.

For the study of wave excitation and propagation, it is convenient to use the plasma conductivity tensors obtained from the linearized equations. The conductivity along the magnetic field  $\sigma_{\parallel}$  is determined by the electron and ion mobilities, and the high parallel conductivity serves to

short-circuit the parallel electric field. The Hall conductivity  $\sigma_H$  dominates over the Pedersen conductivity  $\sigma_p$  in the D and E regions, and the reverse is the case at higher altitudes.

For one ion specie, the Pedersen, Hall, and parallel conductivities are

$$\sigma_p = e^2 \left[ \frac{n_e v_{en}}{m_e (v_{en}^2 + \omega_{ce}^2)} + \sum_i \frac{n_i v_{in}}{m_i (v_{in}^2 + \omega_{ci}^2)} \right] \quad (3.6)$$

$$\sigma_H = e^2 \left[ \frac{n_e \omega_{ce}}{m_e (v_{en}^2 + \omega_{ce}^2)} - \sum_i \frac{n_i \omega_{ci}}{m_i (v_{in}^2 + \omega_{ci}^2)} \right] \quad (3.7)$$

$$\sigma_{\parallel} = e^2 \left( \sum_i \frac{n_i}{m_i v_{in}} + \frac{n_e}{m_e v_{en}} \right) \quad (3.8)$$

The plasma dielectric function  $\epsilon$  is given by

$$\epsilon = \frac{c^2}{V_A^2(z) [1 + v_{in}^2(z) / \omega_{ci}^2]} \quad (3.9)$$

where  $V_A = B / \sqrt{4\pi n_i m_i}$  is the Alfvén speed. Equations (3.1) to (3.9) provide a model for describing wave generation in the ionosphere by HF heating, and the cases for high and mid latitudes are discussed below.

### 3.3. HEATING IN THE HIGH-LATITUDE IONOSPHERE

In the high-latitude region the magnetic field is assumed to be vertical and the propagation of hydromagnetic waves can be separated into the Alfvén and magnetosonic modes in terms of the field variables  $Q = \nabla_{\perp} \cdot E_{\perp}$  and  $M = (\nabla_{\perp} \times E_{\perp}) \cdot \hat{z}$ , respectively. The wave equations can then be written in a convenient form [Lysak, 1997]. The contributions to the external source

$$S_{ext} = -\nabla p_e / m_e$$

can be separated similarly as

$$Q_{ext} = \frac{m_e}{e} \nabla_{\perp} \cdot S_{ext,\perp} \quad \text{and} \quad M_{ext} = \frac{m_e}{e} (\nabla_{\perp} \times S_{ext,\perp}) \cdot \hat{z} \quad (3.10)$$

The wave equations can then be derived from the linearized forms of Equations (3.1) to (3.4) as

$$\epsilon \frac{\partial Q}{\partial t} = -\sigma_p Q \mp \sigma_H M - \frac{\partial J}{\partial z} + \sigma_{p,e} Q_{ext} \pm \sigma_{H,e} M_{ext} \quad (3.11)$$

$$\epsilon \frac{\partial M}{\partial t} = -\sigma_p M \pm \sigma_H Q - \frac{1}{\mu_0} \nabla^2 B_z + \sigma_{p,e} M_{ext} \mp \sigma_{H,e} Q_{ext} \quad (3.12)$$

$$\frac{\partial B_z}{\partial t} = -M \quad (3.13)$$

$$\frac{\partial J}{\partial t} = -\frac{1}{\mu_0} \frac{\partial Q}{\partial z} + \frac{1}{\mu_0 \sigma_{\parallel}} \nabla_{\perp}^2 J + \frac{\sigma_{\parallel,e}}{\mu_0 \sigma_{\parallel}} \frac{\partial Q_{ext}}{\partial z} \quad (3.14)$$

The  $\pm$  corresponds to the magnetic field direction, namely upward ( $-$ ) and downward ( $+$ ). The conductivities  $\sigma_{p,e}$ ,  $\sigma_{H,e}$ , and  $\sigma_{\parallel,e}$  are the electron components of the corresponding expressions defined by Equations (3.6) to (3.8).

The wave propagation model described above yields a framework for the simulation of low-frequency waves in the ionosphere. A two-dimensional (2D) version of the simulation code is implemented in cylindrical geometry with the  $z$ -axis along the magnetic field, taken to be vertical for the high-latitude region. The heated region is modeled as an azimuthally symmetric pancake-shaped region, with a profile given by Equation (3.5). In the numerical implementation discrete Fourier–Bessel transforms are used in the radial direction and the Crank–Nicholson scheme is used in the  $z$ -direction and for advancing in time. An advantage of this implementation is that the numerical stability is not limited by the Courant condition and the equations can be solved for the neutral atmosphere. This enables a smooth transition from the ionosphere to the atmosphere and thus provides the fields on the ground directly. A typical size of the simulation box is 1000 km  $\times$  1000 km.

#### 3.3.1. Waves Generated by Modulated HF Heating: Ionospheric Current Drive

The modeling of HF heating shows the generation of hydromagnetic waves by a two-step process. Figure 3.2 shows a snapshot of the magnetic field components ( $B_r$ ,  $B_{phi}$ ,  $B_z$ ), electric field components ( $E_r$ ,  $E_{phi}$ ), and current density  $J_z$  excited by a heated region with  $L_z = 40$  km, and  $L_r = 20$  km located at  $z = 300$  km and modulated at 5 Hz. The ionosphere is represented by a Chapman profile with a peak density of  $5 \times 10^{10} \text{ m}^{-3}$ , corresponding an Alfvén speed of 900 km/s. The perturbations generated by the heating are dominantly compressional, as shown by ( $B_r$ ,  $B_z$ , and  $E_{phi}$ ) in the left panels of Figure 3.2. The diamagnetic current is in the azimuthal direction, and the compressional components it produces propagate mainly in the transverse direction. These perturbations propagate down to the region where Hall conductivity dominates, and become dominantly shear type, shown by ( $B_{phi}$ ,  $E_r$ , and  $J_z$ ) in the right panels of Figure 3.2. An advantage of

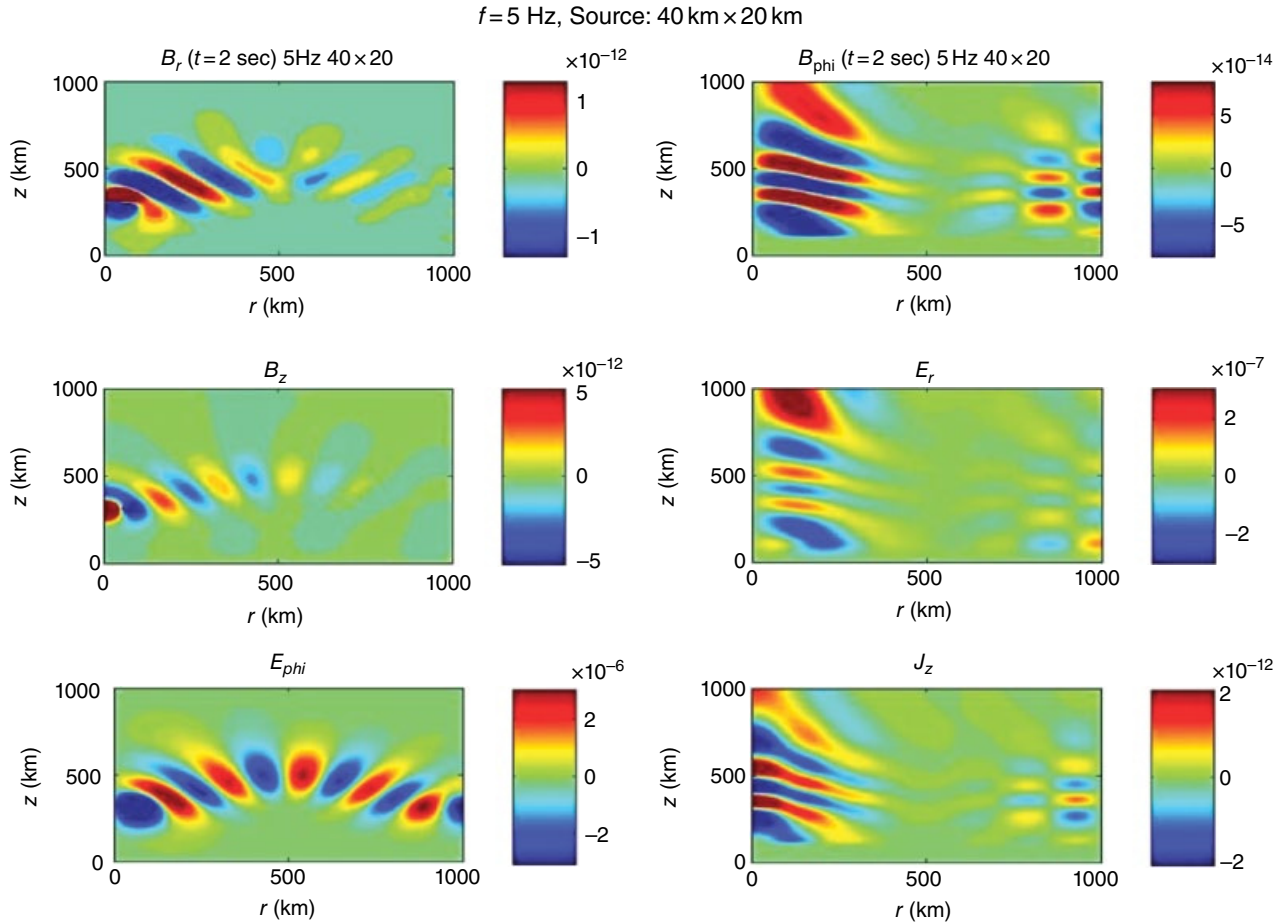


**Figure 3.2** Magnetic field components ( $B_r$ ,  $B_{\phi}$ ,  $B_z$ ), electric field components ( $E_r$ ,  $E_{\phi}$ ), and current density  $J_z$  excited by a heated region with  $L_z = 40$  km, and  $L_r = 20$  km located at  $z = 300$  km and modulated at 5 Hz. A Chapman profile with a peak density of  $5 \times 10^{10} \text{ m}^{-3}$  (Alfvén speed of 900 km/s) was used and the snapshots show the spatial structure at  $t = 2.0$  s after the heating is turned on.

this code is the seamless transition from the ionospheric plasma to the neutral atmosphere, and this enables a proper computation of the fields on the ground. The waves generated near ( $r \approx 0$ ,  $z \approx 300$  km) are reflected ( $r \approx 500$  km,  $z \approx 500$  km) and propagate to  $r \approx 1000$  km on the ground. The shear Alfvén waves are generated by the fast mode in the altitudes regions with  $\sigma_H > \sigma_P$  (Figure 3.1) and propagate to the magnetosphere. This mechanism of generating low-frequency waves is referred to as the ionospheric current drive (ICD) and is shown schematically in Figure 3.3. The essential elements in this mechanism are the time-dependent current that excites the magnetosonic mode and the change in the relative role of the conductivities with altitude. A similar mechanism works in the case of a rocket. The exhaust in the early stage and its ascent can be a source of time-varying current and the generation of Pc1 waves in the ionosphere [Pilipenko *et al.*, 2005].

A series of experiments were conducted using the HAARP ionospheric heater to test and validate the ICD concept, and determine its constraints and scaling properties with ELF frequency, HF power and polarization [Papadopoulos *et al.*, 2011b]. The experiments focused on the dependence on ELF frequency, HF polarization, and HF power; the results are summarized in Figure 3.4. Waves between 0.1 and 70 Hz were detected at both the near and far sides of the heater. Unlike the PEJ, which favors X-mode heating, the ICD amplitude is found to be independent of the polarization of the HF heating wave. From among the frequencies used to modulate the HF waves, 11 Hz showed the maximum amplitude of the generated ELF waves, and their spectrum had a  $1/f$  dependence at higher frequencies up to 70 Hz. Further, it was found that the amplitude of the ELF/ULF signals scaled linearly with power, similar to PEJ generation.

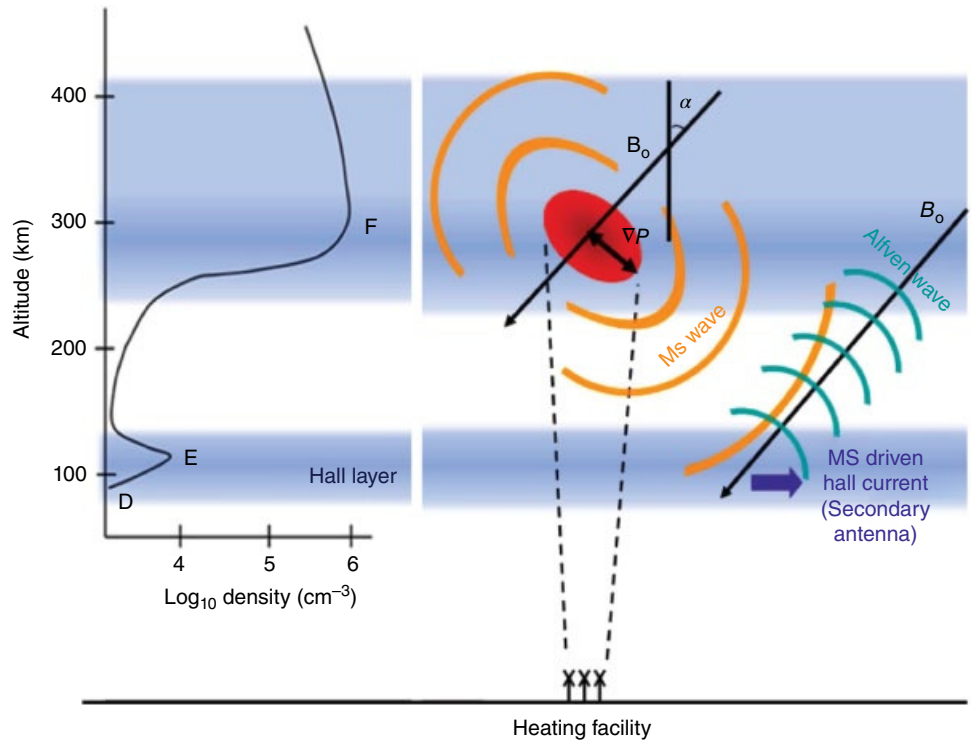


**Figure 3.3** Ionospheric current drive (ICD) physics. A modulated HF heating (red patch) creates diamagnetic currents that excite magnetosonic (MS) waves. In the Hall layer, these waves lead to local currents that excite shear Alfvén waves. From *Papadopoulos et al.* [2011a].

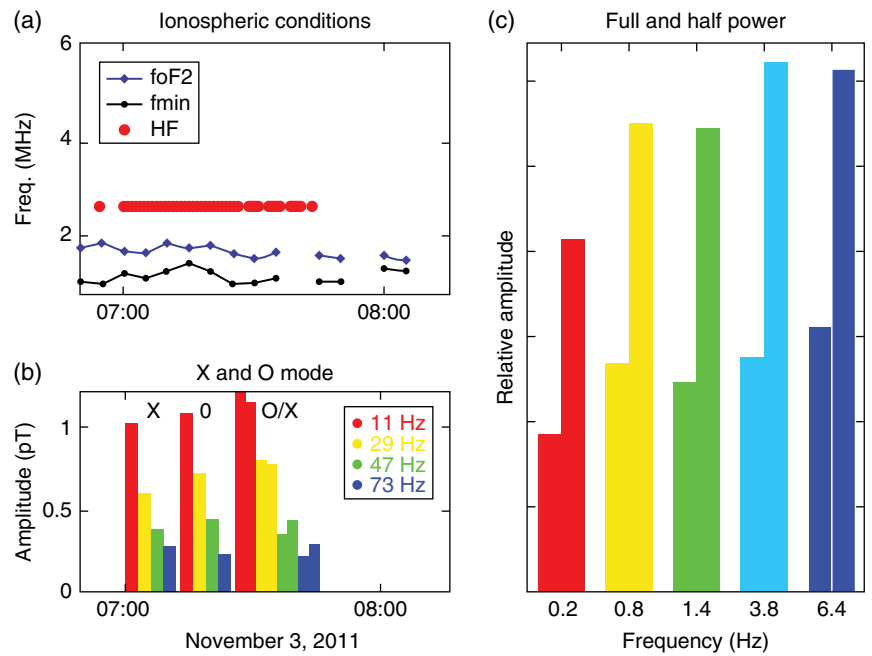


**Figure 3.4** (a) ICD features for during experiments under stable conditions. (b) ELF amplitudes showing no dependence on polarization (O, X and O/X) but  $1/f$  dependence. (c) Amplitude scales with HF power in which the first half is 50% of the second half. From *Papadopoulos et al.* [2011b].



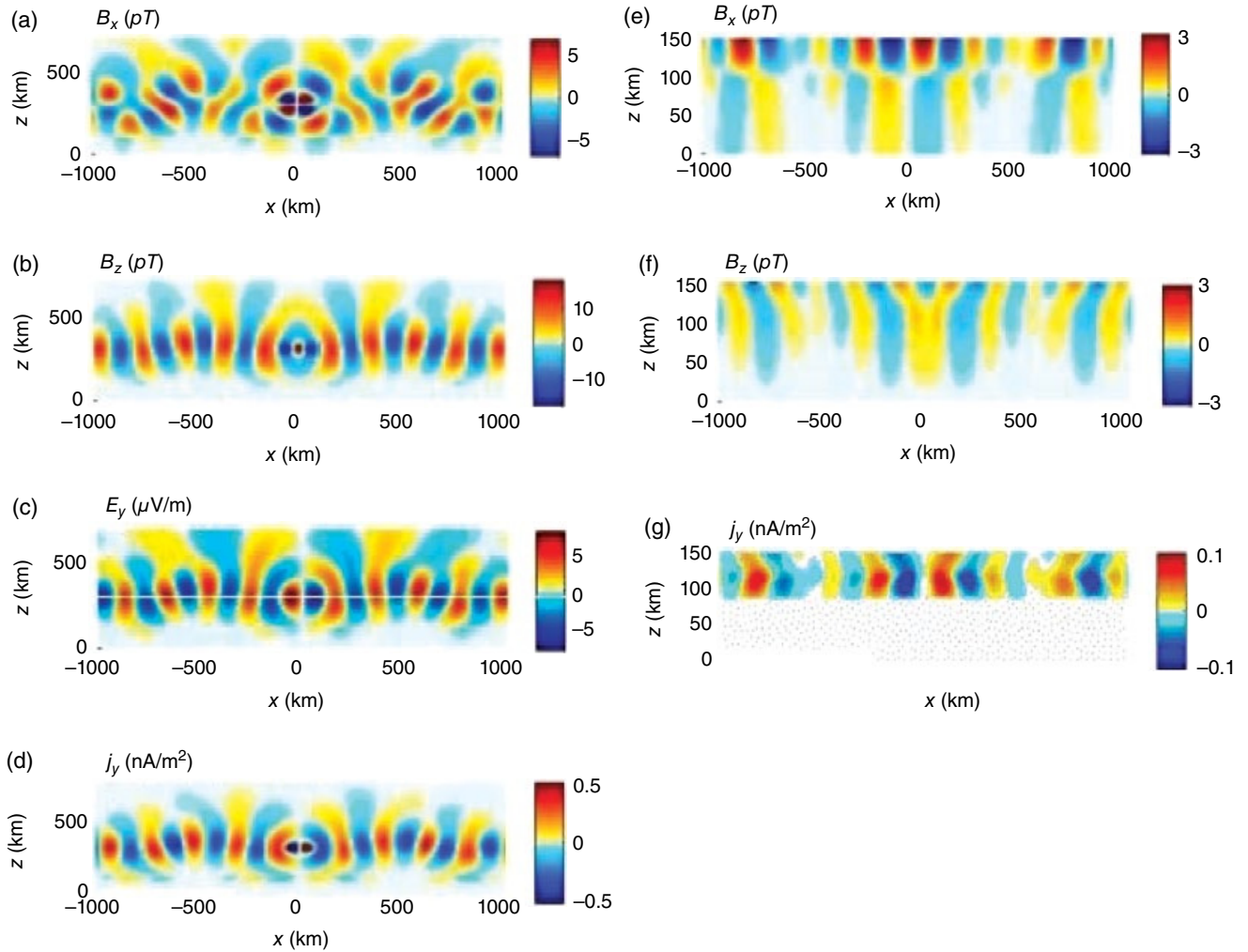


**Figure 3.5** Magnetosonic wave propagation at  $t = 5$  s in HF heating of high-latitude ionosphere with a modulation frequency of 2 Hz. (a, b) The  $x$ - and  $z$ -components of the magnetic field ( $\rho T$ ); (c, d) the associated  $y$ -components of the electric field ( $\mu\text{V/m}$ ) and current density ( $\text{nA/m}^2$ ); (e–g) close-ups of  $B_x$ ,  $B_z$ , and  $j_y$  below 150 km and in free space below 90 km. From *Eliasson et al.* [2012].

Another set of two-dimensional simulations of heating and associated wave generation in the ionosphere using the collisional Hall–MHD model, Equations (3.1) to (3.4), has yielded more details of the physical processes that can be compared with the ICD experiments. The simulations used a model ionosphere (Figure 3.1) and a 2 Hz modulation of the electron pressure [*Eliasson et al.*, 2012]. The ionospheric density maximum and the corresponding Alfvén speed minimum was at an altitude of 300 km, which constitutes the ionospheric waveguide for magnetosonic waves. To model high-latitude conditions, the geomagnetic field is directed vertically downward. In the E region below 120 km, the ions are strongly coupled to the neutral species, and the Hall conductivity dominates the dynamics. The plasma there supports whistler-like helicon waves below the ion cyclotron frequency, which can lead to

mode conversion between magnetosonic and shear Alfvén waves. The nature of this mode is essentially the same as that of the gyrotropic MHD in an analysis of a slab model of the equatorial ionosphere [*Surkov et al.*, 1997].

Snapshots of the electromagnetic wave fields for a vertical geomagnetic field,  $\theta = 180^\circ$ , are shown Figures 3.5 and 3.6, at  $t = 5$  s after the transmitter has been turned on. The main features, seen in Figure 3.5, are magnetosonic waves that are propagating horizontally in each direction away from the heated region at  $x = 0$ , with the Alfvén speed minimum near  $z = 300$  km. For the ionospheric profiles used in these simulations the Alfvén speed at  $z = 300$  km is approximately  $4 \times 10^5$  m/s, this value yields a wavelength of about 200 km for 2 Hz, in agreement with the simulations shown in Figure 3.5. The magnetosonic waves are primarily associated with the compression and



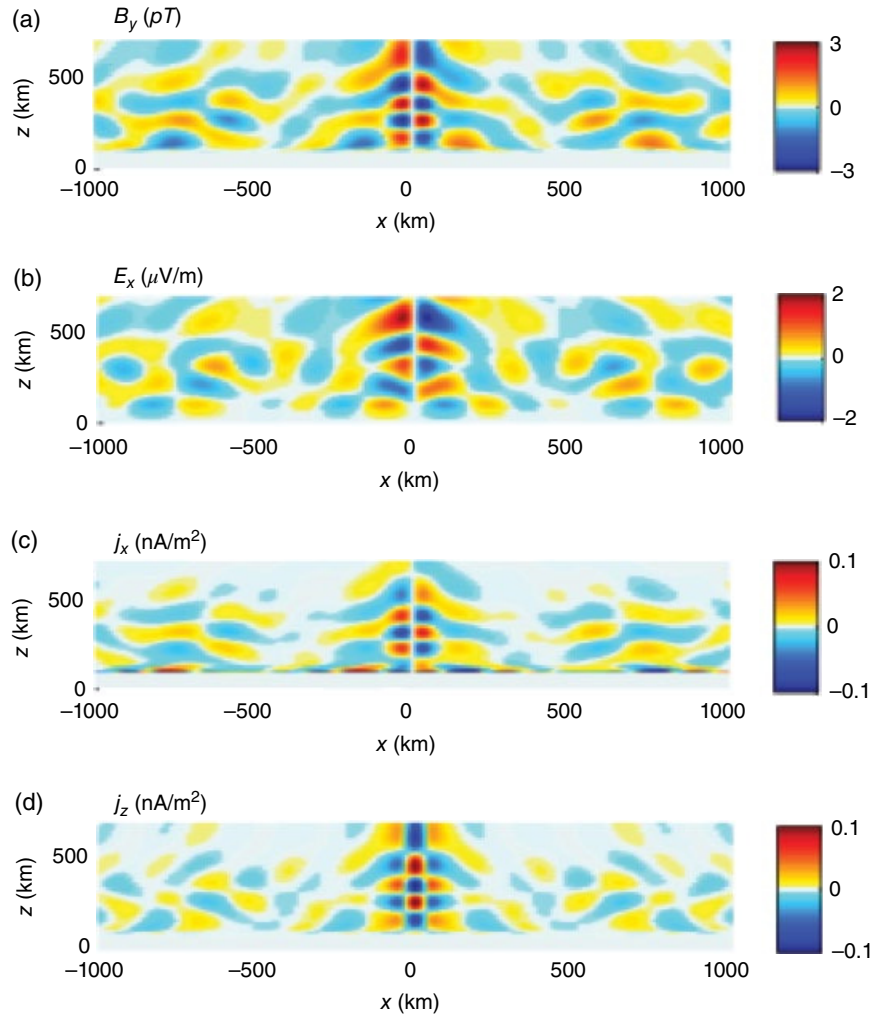


**Figure 3.6** Shear Alfvén wave propagation at  $t = 5$  s in the simulations shown in Figure 3.5. The shear Alfvén wave is associated with (a) the  $y$ -component of the magnetic field in panel, (b) the  $x$ -component of the electric field, and (c, d) the  $x$ - and  $z$ -components of the current density. From *Eliasson et al.* [2012].

rarefaction of the total magnetic field, and hence with the  $z$ -component of the wave magnetic field and the associated  $y$ -components of the electric field and current density. As seen in Figures 3.5a and 3.5b, the magnetosonic wave is associated with a wave magnetic field  $B_z \approx 10$  pT and electric field  $E_y \approx 5 \mu\text{V/m}$ . Below 150 km, shown in Figure 3.6d, the structure of the wave magnetic field changes rapidly, and their amplitudes decrease by a few multiples. These changes in the magnetic field are associated with localized currents in the  $y$ -direction, visible in Figure 3.5g. These currents also generate magnetic fields in free space below 90 km and down to ground, as seen in Figure 3.5e.

The shear Alfvén waves propagate vertically in a narrow column above the heated region along the magnetic field lines, as seen in Figure 3.6. The shear Alfvén waves in the two-dimensional simulation geometry are

associated with the  $y$ -component of the magnetic field, the  $x$ -component of the electric field, and the  $x$ - and  $z$ -components of the current density. The generation of shear Alfvén waves is partially due to mode conversion of magnetosonic waves via Hall currents in the E region, and these waves can also be directly generated in the heated region in the Hall–MHD model, but shear Alfvén waves would not be generated by the modulation of the electron pressure in an ideal MHD model.

The simulations provide the details of the low-frequency waves suitable for a comparison with the observations [*Eliason et al.*, 2012]. In a typical experiment (October 30, 2010, 06:00:00–06:19:30 UT), HAARP transmitted at 2.8 MHz, O-mode, at peak power (3.6 MW), an amplitude modulated square waveform at 2.5 Hz, with the heater beam pointing along the magnetic zenith direction. The local VHF riometer

showed low absorption at  $\sim 0.2$  dB at 30 MHz. The onsite fluxgate magnetometer showed flat traces with no fluctuation, indicating a very quiet ionosphere. The onsite digisonde showed foF2 at 1.45 MHz and F-peak at 260 km altitude with extremely weak E-layer. Figure 3.7 shows the wave spectrum measured simultaneously on the ground approximately 20 km away from the HAARP heater and by the overflying DEMETER. The top left diagram in the figure is a projection of the DEMETER orbit (at 670 km altitude) moving with respect to the HAARP magnetic zenith (MZ). The red marking on the orbit represents the orbit segment during which there was a strong signal at the injected frequency. The time duration was 20 to 25 seconds, which corresponds to a distance of 100 to 150 km. A key aspect of this observation is the strong confinement of the ELF waves to the magnetic filled flux tube, as expected from shear Alfvén waves and as seen in the simulation in Figure 3.6. In another experiment using 0.1 Hz modulation, DEMETER detected generated waves for a duration that was approximately six times longer and allowed for the measurement of the waveform of the electric field, which is identified with a magnetosonic wave that propagates isotropically along the ionospheric waveguide, as seen in the simulation results (Figure 3.5).

An unexpected result revealed by the simulations is the distribution of the ELF magnetic amplitude on the ground signatures as a function of distance from the heater [Eliason *et al.*, 2012]. Previous results with ELF and ULF waves generated by modulating the polar electrojet (PEJ) [Rietveld *et al.*, 1984, 1987, 1989; Papadopoulos *et al.*, 1990, 2005; Moore, 2007; Payne *et al.*, 2007] indicated that the wave amplitude had a maximum in the vicinity of the heater while monotonically decreasing with distance in a fashion consistent with guided wave propagation. In general, ICD driven waves have a minimum at the ground location defined by its intersection with the magnetic field line that passes through the heated volume. However, a HAARP test conducted under daytime conditions during the period 17–25 August 2009 measured magnetic signals simultaneously in Gakona and in Homer 300 km away. A number of frequencies between 12 and 44 Hz were generated and simultaneously measured at the two sites. The signals generated by PEJ were found to be larger in Gakona than in Homer, which is consistent with previous PEJ observations. But the situation is reversed for the remaining signals, associated with ICD, and many were detected only in Homer and not in Gakona. This, as explained previously and seen in the simulations, is a result of the two-step ELF generation by ICD. In particular, the Hall current that acts as a secondary antenna that generates the ground signals occurs at the location where the magnetosonic wave reaches the Hall region. As a result the minimum occurs

at the intersection of the magnetic field line with ground and the maximum at a distance that depends on the heating altitude and the geomagnetic latitude.

The efficiency of wave generation is affected by the plasma conditions prevailing in the heated region, and to explore this, Milikh and Papadopoulos [2007] developed a model in which two time-scale heating periods were used. In this approach a minute-long heating pulse is followed by another period of heating with modulation at the desired ELF/VLF frequency. The long pulse reduces the electron-ion recombination coefficient, resulting in increased ambient electron density and current density. It was observed that following the long preheating pulse by amplitude modulated heating at VLF frequencies, increases of wave intensity can result by up to 7 dB over the case of no preheating. An extensive campaign of heating experiments [Cohen and Golkowski, 2013] provided some evidence that such a preheating effect occurred at HAARP, where the 5 dB increase of median VLF amplitude was detected (Figure 3.8). The estimates on the median ELF power radiated by HAARP to the waveguide mode show that the preheating could reach 1 W at 250 km, if the geometric modulation circle sweep is applied.

### 3.3.2. Generation of Whistler Waves by Continuous HF Heating of the F Region

In addition to wave generation by modulated heating, whistler wave can be generated by *continuous* ionospheric heating. Experiments by Vartanyan *et al.* [2016] reveal a mechanism that injects broadband ( $\Delta f/f \approx 0.1-0.25$ ) whistler waves into the magnetosphere in the absence of electrojet currents. During a daytime CW ionospheric heating experiment on 10-16-2009 (experiment 1), whistler waves in the VLF frequency range 7–10 kHz and 15–19 kHz were detected by the overflying DEMETER satellite during its closest approach to the HAARP MZ. Similarly, whistler waves were detected during a daytime 0.7 Hz modulated ionospheric heating experiment on 02-10-2010 (experiment 2), but only in the latter frequency range of 15–19 kHz. Figure 3.9 shows the spectrograms observed by DEMETER during experiments 1 (Figure 3.9a) and 2 (Figure 3.9b) as it made its closest flyby of the HAARP MZ at  $t = 0$ .

In both experiments the HAARP heater operated at its maximum 3.6 MW power with a MZ-oriented O-mode HF beam, and the heating frequencies used were 5.1 MHz ( $f_oF_2$ ) and 4.25 MHz ( $\lesssim 3f_{ce}$ ) for experiments 1 and 2, respectively. Note that the frequency range of the whistler waves corresponds to the F region lower-hybrid (LH) frequency and its second harmonic, suggesting that parametrically excited LH waves at the upper hybrid layer were mode-converted into whistler waves. For the

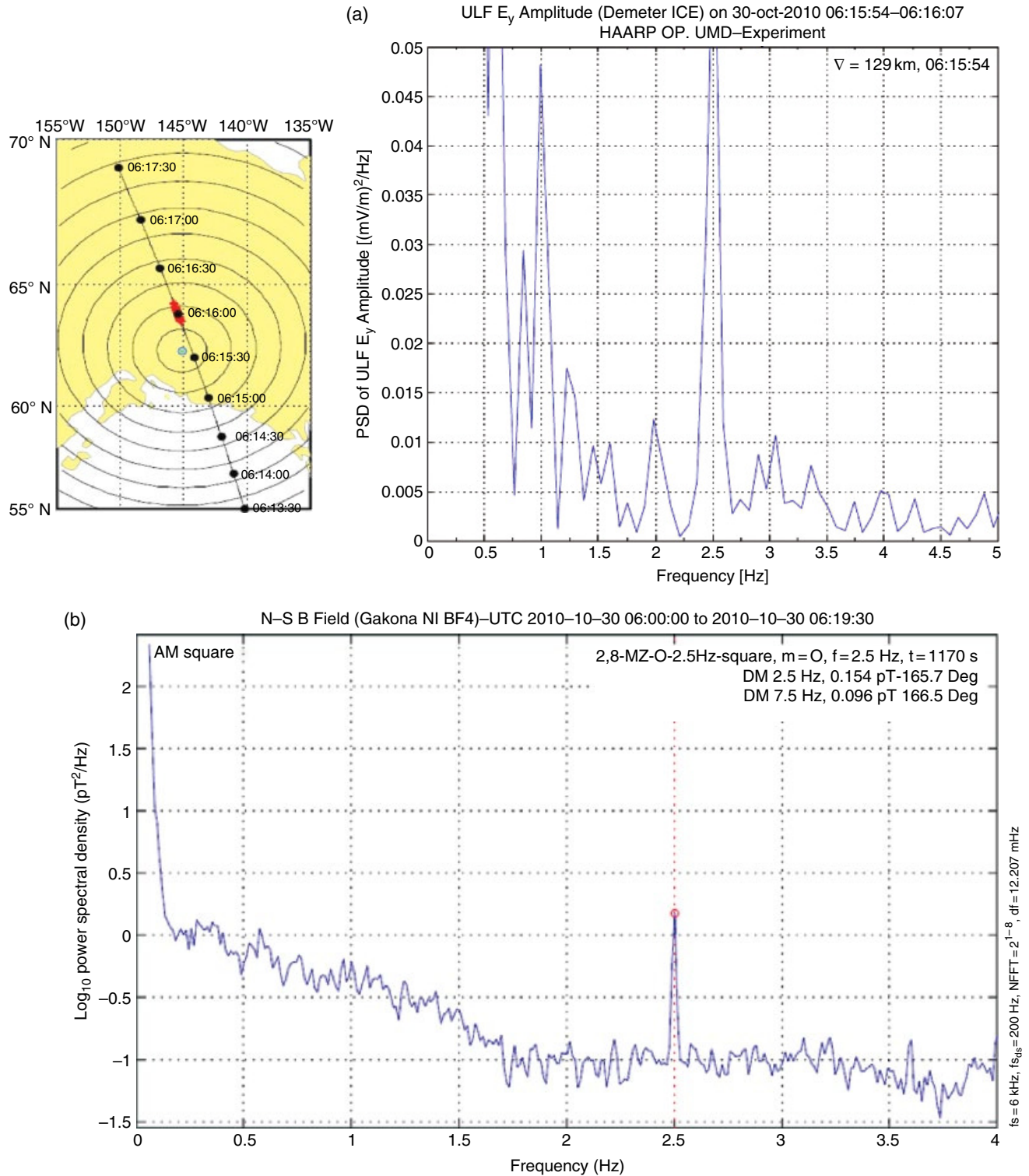


**Figure 3.7** (a) Electric field spectrum measured by DEMETER during 2.5 Hz modulation of the HAARP heater. The heater was operated at full power (3.6 MW), 2.8 MHz frequency, and O-mode polarization. The top left diagram indicates the DEMETER location with respect to the HAARP MZ. (b) Magnetic field spectrum measured at Gakona simultaneously with DEMETER. From *Eliasson et al.* [2012].



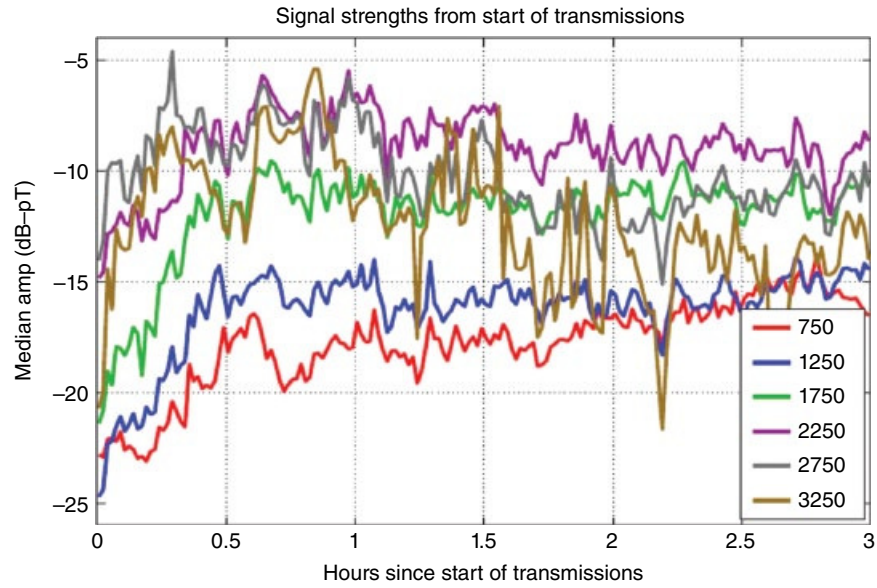


**Figure 3.8** Median amplitudes as a function of the time since transmission began on each day, parametrized by six 500 Hz bins. An increase in the median amplitude by ~5 dB that occurs gradually over the first 30 min is imminent. From *Cohen and Golkowski* [2013].

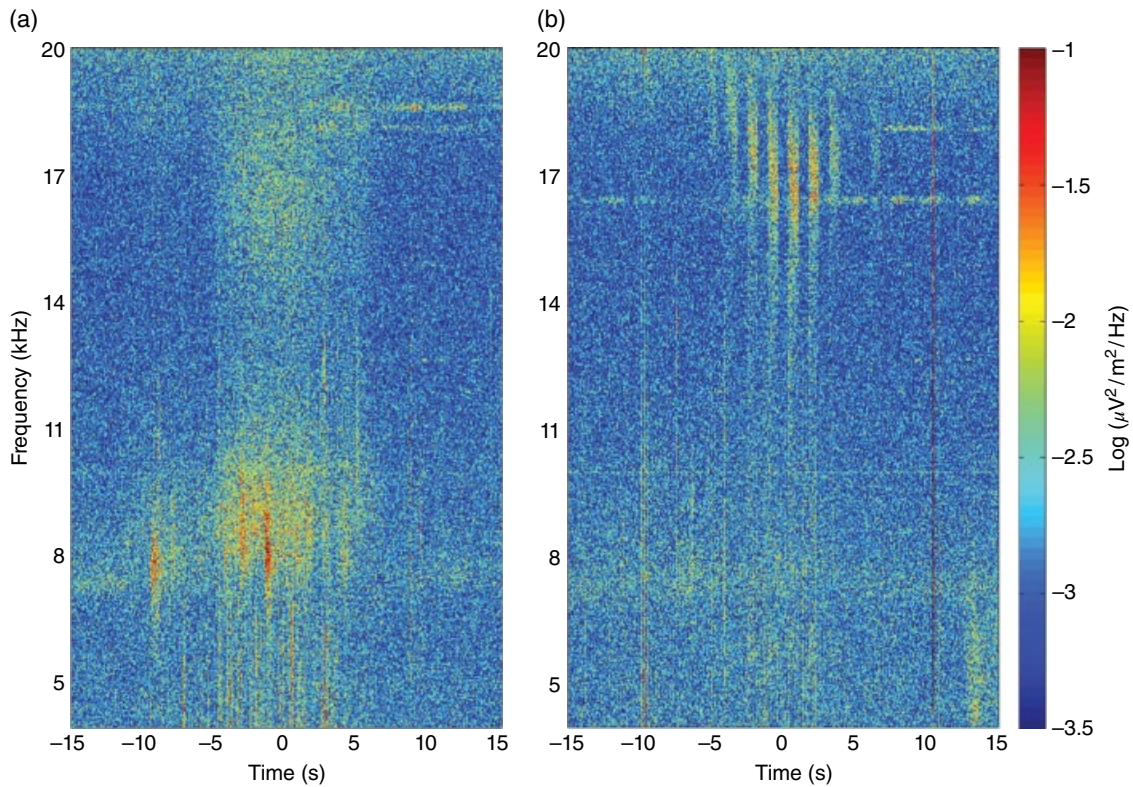


**Figure 3.9** Spectrogram seen by DEMETER during experiment 1 on 16 October 2009 in which HAARP used CW heating (a), and during experiment 2 on 10 February 2010 (b) in which HAARP used 0.7 Hz square pulse modulated heating. In both cases  $t = 0$  corresponds to the closest approach of DEMETER to the HAARP MZ. From *Vartanyan et al.* [2016].

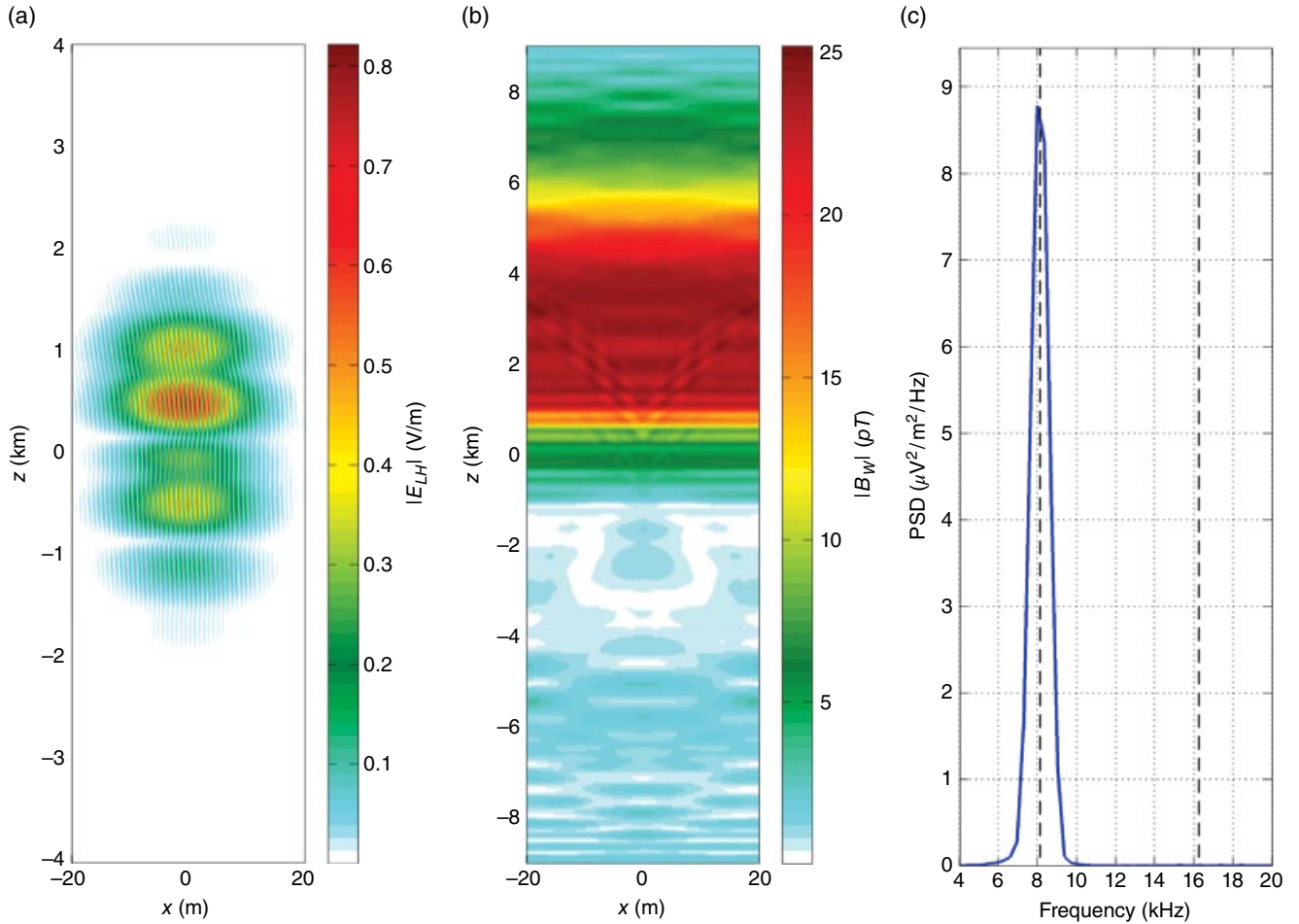


**Figure 3.10** Simulation results showing a LH wave packet mode converting to whistler waves of the same frequency, by interacting with an external striation. (a) The magnitude of the LH electric field in V/m, (b) magnitude of the whistler magnetic field in pT, and (c) spectrum of the  $y$ -component whistler electric field in  $\mu\text{V}^2/\text{m}^2/\text{Hz}$ ; the vertical lines in (c) represent the LH frequency and its second harmonic. From *Vartanyan et al.* [2015].

above-mentioned heating settings, LH waves are known to be generated by parametric instabilities that are triggered by the HF–pump–plasma interactions. This is confirmed by SEE observations (not shown here) available during experiment 2 [*Vartanyan et al.*, 2016].

Based on the proposed mechanism, the observed VLF with frequencies near the LH frequency were generated by resonant mode conversion of LH waves to whistler waves [*Eliasson and Papadopoulos*, 2008] in the presence of artificially pumped meter-scale striations, as one would expect during long-term CW heating in the case of experiment 1. A simulation of this can be performed by using the LH–whistler mode conversion model developed by *Eliasson and Papadopoulos* [2008], as shown in Figure 3.10. The figure reveals a LH wave packet (Figure 3.10a) interacting with an external field aligned (vertical) striation and generating whistler waves (Figure 3.10b), whose frequency spectrum has a large

peak at the LH frequency (Figure 3.10c). Note, however, that whistler waves near the LH frequency were not detected during experiment 2. This is because the 0.7 Hz (0.7 s on, 0.7 s off) modulated HF heating pulses did not allow a sufficiently long time to develop significant meter-scale striations, thus preventing an efficient linear coupling from LH waves to whistlers.

The VLF near the LH harmonic observed during both experiment 1 (CW) and experiment 2 (pulsed heating) was shown to be generated by a different mechanism: the nonlinear interaction of counterpropagating LH waves. While in the first mechanism LH waves linearly coupled to whistler waves via the external irregularities (striations), this mechanism relies on LH waves nonlinearly coupling to whistler waves via the density fluctuations of another (counterpropagating) LH wave, and as such *does not* directly rely on striations. Using the above-mentioned LH–whistler mode conversion

model with two counterpropagating LH waves, but generalizing the model to include the nonlinear coupling, this mechanism could be simulated to yield whistler waves at the LH harmonic [Vartanyan *et al.*, 2016]; the simulation was achieved by placing two counterpropagating LH waves on top of each other and observing the spectrum of the subsequently mode-concerted whistlers. Since the only requirement for the mechanism is the presence of LH waves (known to be generated in less than 20 ms), whistler waves were indeed observed by DEMETER during both experiments. If the two simulations were combined into one, then the frequency spectrum would reveal peaks at both the LH frequency and its harmonic [Vartanyan *et al.*, 2016], as in the observations (Figure 3.9a).

### 3.4. HF HEATING IN THE MID-LATITUDE IONOSPHERE

The mid-latitude ionosphere has features, such as the curvature of Earth's dipole magnetic field and the absence of a steady current system, that lead to physical processes different from those of the high-latitude region. Simulations of the mid-latitude region thus require a model that takes these differences into account, and for HF heating the magnetic field geometry is expected to generate new effects, such as the propagation of the waves into the magnetosphere. A generalized model is derived from Equations (3.1) to (3.4) [Eliasson *et al.*, 2012]:

$$\frac{\partial \mathbf{A}}{\partial t} = -\mathbf{E} \quad (3.15)$$

and

$$\begin{aligned} \frac{\partial \mathbf{E}}{\partial t} = & -\omega_{ci} (\Gamma_{in} + \Gamma_{en}) \mathbf{E} + \frac{\bar{\bar{\epsilon}}^{-1} [\nabla \times (\nabla \times \mathbf{A})]}{\mu_0} \\ & - \frac{\bar{\mathbf{R}}_e [\nabla \times (\nabla \times \mathbf{E})]}{\mu_0 \bar{\sigma}} + \left( \omega_{ci} \bar{\mathbf{R}}_i - \frac{\partial}{\partial t} \right) \frac{\nabla P_e}{en_0} \end{aligned} \quad (3.16)$$

where we introduce the vector and scalar potentials  $\mathbf{A}$  and  $\phi$  via  $\mathbf{B} = \nabla \times \mathbf{A}$  and  $\mathbf{E} = -\nabla \phi - \partial \mathbf{A} / \partial t$ , using the gauge  $\phi = 0$ . The  $\bar{\mathbf{R}}_e$  and  $\bar{\mathbf{R}}_i$  matrices (organizing the vectors as column vectors) are deduced from the electron and ion equations of motion (3.1) and (3.2) via the definitions  $(\mathbf{v}_e \times \mathbf{B}_0 + m_e v_{en} \mathbf{v}_e / e) / B_0 \equiv \bar{\mathbf{R}}_e \mathbf{v}_e$  and  $(\mathbf{v}_i \times \mathbf{B}_0 - m_i v_{in} \mathbf{v}_i / e) / B_0 \equiv \bar{\mathbf{R}}_i \mathbf{v}_i$ , respectively. We can replace the Cartesian coordinate system  $(x, y, z)$  of Eliasson *et al.* (1012) by a spherical coordinate system  $(R, \varphi, \theta)$ , where  $R, \varphi$ , and  $\theta$  are the radial, longitudinal,

and co-latitudinal coordinates, respectively. In spherical coordinates, the magnitude of the dipole magnetic field is  $B_0 = B_{eq} (R_E / R)^3 \sqrt{1 + 3 \cos^2 \theta}$ . The  $\bar{\mathbf{R}}_e$  and  $\bar{\mathbf{R}}_i$  matrices are used to construct the inverse of an effective dielectric tensor  $\bar{\bar{\epsilon}}^{-1} = -(v_A^2 / \varepsilon_0 c^2) \bar{\mathbf{R}}_e \bar{\mathbf{R}}_i$ , where  $v_A = c \omega_{ci} / \omega_{pi}$  is the Alfvén speed, and a conductivity tensor  $\bar{\sigma} = \omega_{ci} (\Gamma_{in} + \Gamma_{en}) \bar{\bar{\epsilon}}$ , which we denote as  $\Gamma_{en} = v_{en} / \omega_{ce}$  and  $\Gamma_{in} = v_{in} / \omega_{ci}$ . Correspondingly,  $\omega_{ci} = e B_0 / m_i$  and  $\omega_{ce} = e B_0 / m_e$  are the ion and electron cyclotron frequencies,  $\omega_{pi} = (n_0 e^2 / \varepsilon_0 m_i)^{1/2}$  and  $\omega_{pe} = (n_0 e^2 / \varepsilon_0 m_e)^{1/2}$  are the ion and electron plasma frequencies,  $\varepsilon_0 = \mu_0 / c^2$  is the electric permittivity in vacuum,  $c$  is the speed of light in vacuum, and  $\bar{\sigma} = \varepsilon_0 \omega_{pe}^2 / \omega_{ce}$ .

The mid-latitude ionosphere has similar plasma profiles as the auroral region, but the magnetic field geometry is significantly different in at least two ways. As shown in Figure 3.11, the field lines are oblique and curved, and this can lead to changes in the propagation characteristics of the waves. For example, a wave front propagating out of a heated region in the mid-latitude ionosphere will intercept a wider area in the E region where the shear Alfvén waves are excited.

The simulations were conducted in a domain in the north-south plane in the spherical coordinates covering  $R = R_E + 100$  km to  $R_E + 4000$  km in the radial direction and a region  $90^\circ$  wide angular region in the co-latitudinal direction centered at the foot of the  $L = 1.6$  shell, namely  $\arcsin(1/\sqrt{L}) - 45^\circ \leq \theta \leq \arcsin(1/\sqrt{L}) + 45^\circ$ . This domain is the region shaded in green in Figure 3.11. The simulation was run up to 12 seconds using  $4 \times 10^5$  timesteps. The ionosphere was represented by a Chapman profile, with a peak density of  $5 \times 10^{10} \text{ m}^{-3}$  at about 500 km, corresponding to a minimum of the Alfvén speed of  $v_A \approx 900$  km/s. The simulation domain was resolved with 500 cells in the

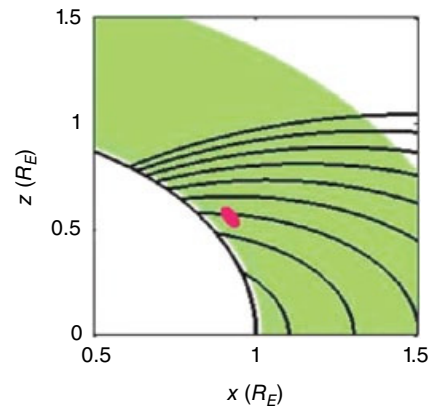


**Figure 3.11** Part of the simulation domain (shaded in green) using polar coordinates in the mid-latitude region with the Earth's dipole magnetic field. The heated region (in red) is centered at the magnetic field line  $L = 1.6$ . From Sharma *et al.* [2016].



radial direction and 460 cells in the co-latitudinal direction. A centered second-order difference scheme was used in the radial direction and a pseudospectral method with periodic boundary conditions in the co-latitudinal direction. The simulations were stopped before the waves reached the simulation boundaries in the co-latitudinal direction, hence eliminating the effects of the artificial periodic boundary conditions. First-order outflow boundary conditions were used at the top boundary in the radial direction. At the lower boundary between the plasma and free space at  $R = R_E + 100$  km, we constructed boundary conditions by assuming that the horizontal components of the electric field and vector potential, and their radial derivatives, are continuous. In free space, we assumed infinite speed of light and no electric charges or currents, while the ground at  $R = R_E$  is perfectly conducting. This way analytic approximations for the free space electromagnetic fields could be used (see *Eliasson et al.* [2012]).

In this setup  $T_e$  given by Equation (3.5) peaks in the center of the heated region on the  $L$  shell. In these simulations  $R_E = 6000$  km,  $T_{mod} = 2000$  K,  $D_t = 0.5$  s,  $D_{r\theta} = 40$  km,  $D_h = 20$  km, and  $h_{max} = 300$  km, and  $L = 1.6$ .

The propagation of the low-frequency waves into the magnetosphere, where the magnetic field is significantly

reduced, leads to the possibility of their coupling to other modes, notably the electromagnetic ion cyclotron (EMIC) mode. The roles of these waves can be seen from the dispersion relation for collisionless obliquely propagating ELF Alfvén waves, that is,

$$(\omega^2 - v_A^2 k^2)(\omega^2 - v_A^2 k_{\parallel}^2) - \frac{\omega^2}{\omega_{ci}^2} v_A^4 \kappa^2 \kappa_{\parallel}^2 = 0,$$

where  $k^2 = k_{\parallel}^2 + k_{\perp}^2$ . For perpendicular propagation ( $k_{\parallel} = 0$ ) the solution of the equation above yields the compressional or magnetosonic waves ( $\omega \simeq kv_A$ ). For parallel propagation ( $k = k_{\parallel}$ ) and large wavenumbers  $k \gtrsim c/\omega_{pi}$ , the shear Alfvén mode splits into two modes: the right-hand circularly polarized (R-mode) whistler and the left-hand circularly polarized (L-mode) electromagnetic ion cyclotron (EMIC) mode, also known as the Alfvén cyclotron mode. While the whistler mode can propagate at frequencies  $\omega > \omega_{ci}$  at large wavenumbers, the EMIC propagates at frequencies  $\omega < \omega_{ci}$  and has a resonance at  $\omega_{ci}$  for large wavenumbers.

The HF heating with modulation frequencies  $f = 2$  Hz, 5 Hz, and 10 Hz were simulated. Figure 3.12 shows the

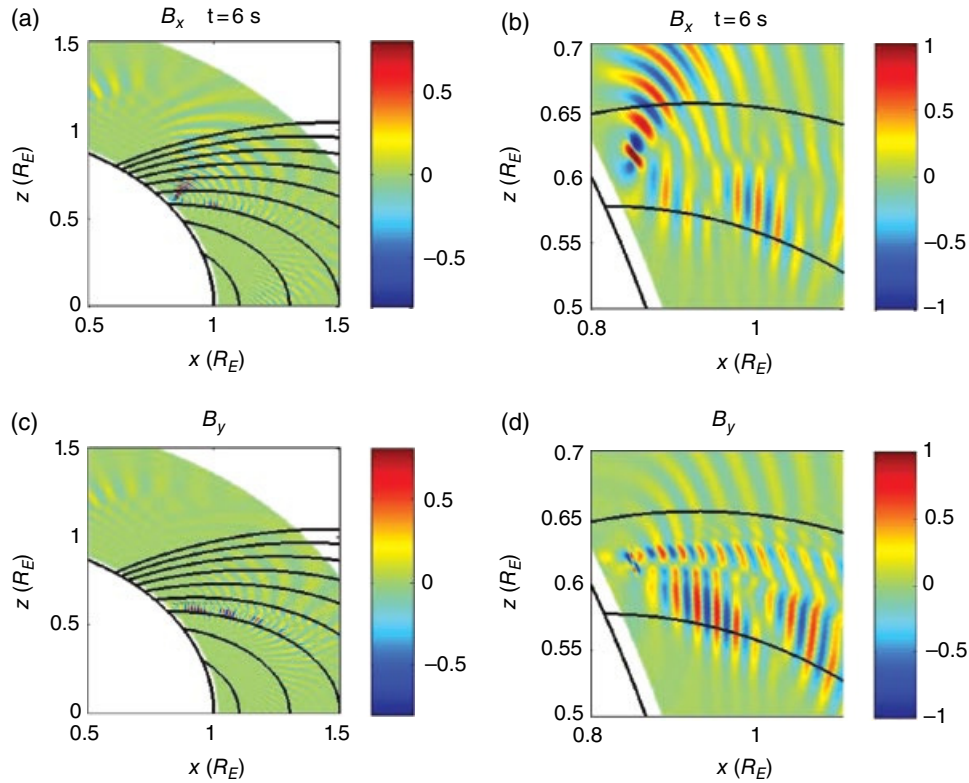


**Figure 3.12** Wave magnetic field (pT) of 5 Hz ELF waves excited by modulated ionospheric heating. The  $B_x$  component (a, b) is associated with magnetosonic waves, while the  $B_y$  component (c, d) is associated with shear Alfvén waves. (b, d) show a close-up of (a, c), respectively, in the heated region. From *Sharma et al.* [2016].



excitation of both magnetosonic and shear Alfvén waves for modulation at 5 Hz. At frequencies much below the ion cyclotron frequency (of the order 10–50 Hz depending on altitude and latitude), the shear Alfvén wave propagates primarily along the magnetic field lines. Magnetosonic waves ( $B_x$ ) are created by ICD and propagate at large angles to the geomagnetic field lines upward to the magnetosphere and downward to E region (Figure 3.12). Somewhat below the  $L = 1.6$  magnetic field line extending from the heated region are whistler mode waves (see Figure 3.12d). These waves are not created at the heated location but at the Hall region at the bottom of the ionosphere where magnetosonic waves have been mode-converted to helicon waves, which propagate to higher altitudes as whistler waves. Near the heated region there is also a direct generation of EMIC waves.

As the wave frequency becomes comparable to the ion cyclotron frequency, the splitting of the shear Alfvén wave into the whistler and EMIC branches become more pronounced. The whistler wave is characterized by a longer wavelength and higher propagation speed than the EMIC wave at a given frequency. This is particularly evident in the modulation at 10 Hz, in which case the shorter wavelength EMIC waves and longer wavelength whistler waves are sharply distinguished in comparison to the less pronounced magnetosonic wave propagating at larger angles to the geomagnetic field. An interesting question is what happens when the EMIC reaches the ion cyclotron

resonance at high altitudes, indicated by thin lines in Figures 3.12a and 3.12c. The simulations show that the 10 Hz EMIC waves cannot propagate beyond the ion cyclotron resonance layer where their wavelength goes to zero, and thus the EMIC wave energy will pile up near the resonance [Sharma *et al.*, 2016].

The HF heating experiments in the mid-latitude ionosphere using the facilities at Arecibo [Ganguly *et al.*, 1986], Platteville [Utlaut *et al.*, 1974], and Sura [Kotik *et al.*, 2013] have provided a range of observations. The Arecibo experiment showed the generation of ULF waves, which have been interpreted as nonlinear coupling of two waves and amplitude modulation of a single wave. The Platteville experiments showed the formation of field-aligned artificial irregularities but no direct evidence of low-frequency waves. The experiment using the Sura facility have provided detailed measurements of low-frequency waves and have been interpreted in terms of a ponderomotive excitation mechanism. The modeling of the Sura experiments using the numerical model presented here will be pursued.

### 3.5. KINETIC PROCESSES IN HF HEATING

The modeling of the excitation of low-frequency waves in HF heating discussed above uses an ionospheric profile, shown in Figure 3.1, that does not include small-scale features, such as striations and

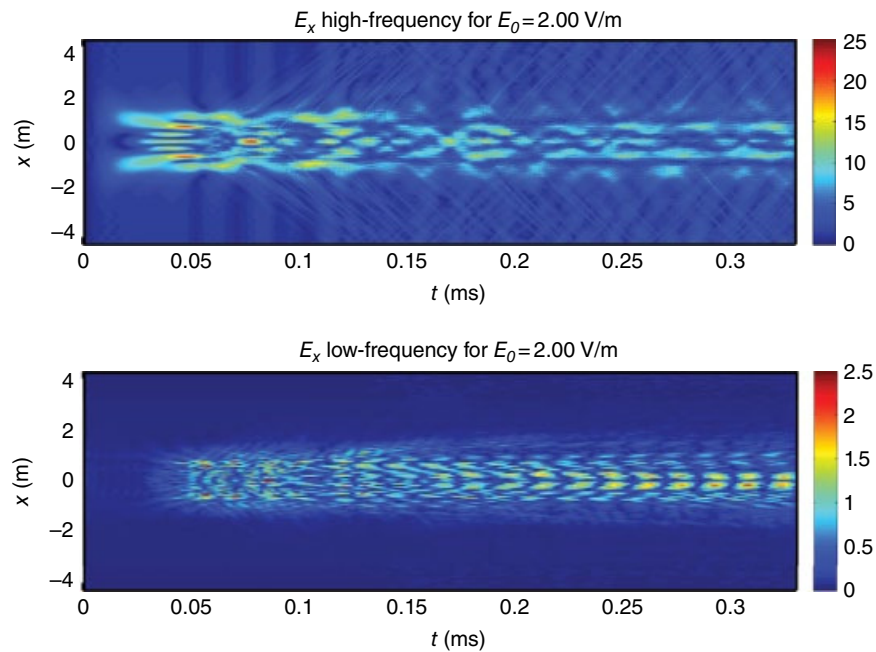


**Figure 3.13** Amplitudes of high-frequency and low-frequency electric fields (V/m) as a function of position and time. While both high- and low-frequency waves appear to be mostly confined within the density striation, there is noticeable leaking of the high-frequency waves into the simulation space. From Najmi *et al.* [2016].

ducts. At altitudes below the turning point of an O-mode pump wave, near the upper hybrid resonance, upper hybrid and lower hybrid turbulence can lead to the formation of field-aligned density striations (FAS). Once FAS are formed, O-mode waves are mode-converted to upper hybrid waves, enhancing the turbulence, leading to anomalous absorption of the pump wave and efficient bulk heating of the electrons. Measurements from the EISCAT heater in Tromsø by *Rietveld et al.* [2003] directly verify the increase in electron temperature by 3000 K whereas the ion temperature was enhanced only by 100 K. Later experiments by *Blagoveshchenskaya et al.* [2011] show electron temperatures reaching close to 6000 K when the HF pump approaches magnetic zenith. Although the experimental facilities at HAARP cannot directly measure electron temperature, they have been able to detect descending artificial ionized layers (DAIL) [*Pedersen et al.*, 2009], the generation and descent of which were modeled extensively by *Eliasson et al.* [2012], indicating that the DAILs required bulk heating of the electrons to  $\sim 4000$  K to be subsequently accelerated by Langmuir turbulence to suprathermal speed and ionize the neutrals.

To better understand the heating near the upper hybrid layer, *Najmi et al.* [2016] carried out Vlasov simulations of HF heating in the upper hybrid resonance region of the ionosphere. The Vlasov equation gives the evolution of the distribution function of a species in position and velocity.

$$\frac{\partial f_\alpha}{\partial t} = \vec{v} \cdot \nabla_x f_\alpha + \frac{\vec{F}_\alpha}{m_\alpha} \cdot \nabla_v f_\alpha = 0$$

with the Lorentz force given by

$$\vec{F}_\alpha = q_\alpha (\vec{E} + \vec{E}_{ext} + \vec{v} \times \vec{B}_0)$$

where  $q$  and  $m$  are the charge and  $\alpha$  denotes the specie. The external electric field is taken to be an oscillating dipole field, along the  $x$ -axis  $\vec{E}_{ext} = \hat{x} E_0 \sin(\omega_0 t)$  at frequency  $\omega_0 = 21.59 \times 10^6 \text{ s}^{-1} \approx 3.44 \text{ MHz}$ , and constant amplitude in space. The constant magnetic field  $B_0$  is directed along the  $z$ -axis. Further, in the electrostatic approximation, we can close these equations with the Poisson equation and the continuity conditions for the charge density, with the particle number density obtained by integrating  $f_\alpha$ . The closed set can be solved in position and velocity space using

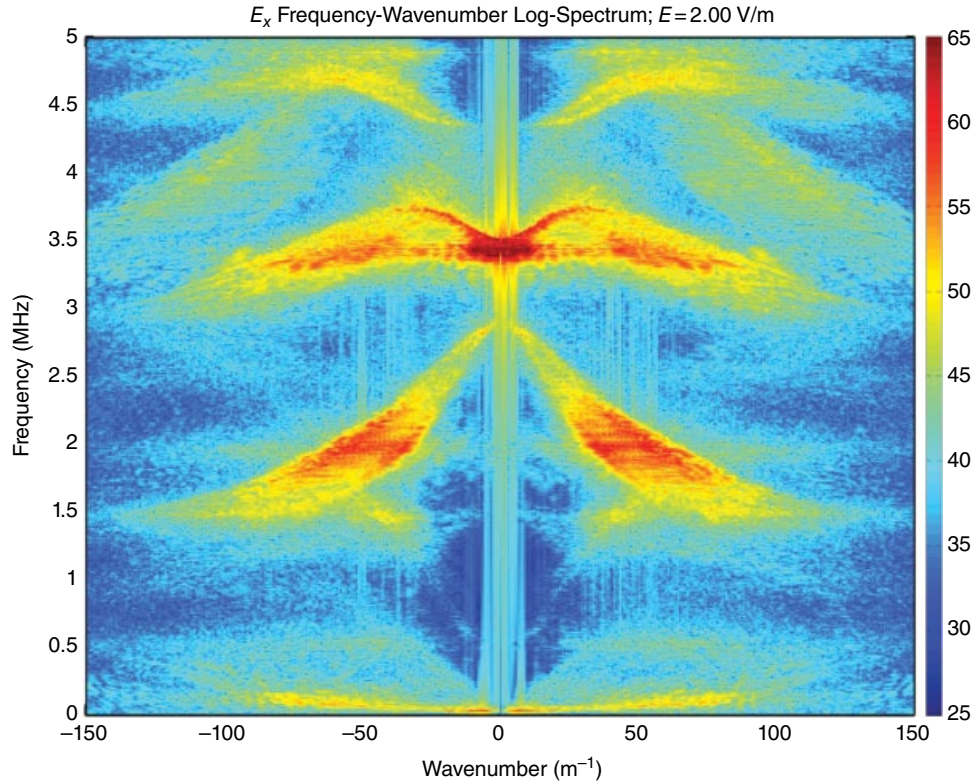


**Figure 3.14** Frequency-wavenumber color map of the electric field. The pump wave is visible near  $k = 0$  and  $f = 3.44$  MHz. The first branch of the electron Bernstein modes are seen near  $k = \pm 50 \text{ m}^{-1}$ ,  $f = 2.0$  MHz, and the second branch at  $|k| < 100 \text{ m}^{-1}$  near  $f = 3.4$  MHz. Lower hybrid waves are visible at  $|k| < 100 \text{ m}^{-1}$  and  $f < 0.1$  MHz. From *Najmi et al.* [2016].

Fourier methods [Eliasson, 2010]. As an initial condition, Najmi *et al.* [2016] used a 10% Gaussian density striation such that the pump frequency was a local upper hybrid resonance at  $n = 0.95n_0$ , corresponding to an FWHM of 2.5 m of the 9 m simulation box. For numerical efficiency an electron-hydrogen plasma was used.

Initially, the dominant waves were a mode-converted pump wave near 3.44 MHz, but low-frequency waves dominated by frequencies close to the lower hybrid frequency of  $\sim 31$  kHz quickly developed. The amplitude of the high-frequency waves inside the striation was about 5 to 10 times larger than the pump amplitude, while the amplitude of low-frequency waves was close to the amplitude of the pump. These components can be seen in Figure 3.13.

A rapid increase of the electron temperature was observed in the simulations [Najmi *et al.*, 2016]. The electron heating was identified as stochastic heating in the presence of large amplitude electron Bernstein and upper hybrid waves, visible in the wave number–frequency–energy spectrum in Figure 3.14.

### 3.6. CONCLUSION

The generation of low-frequency waves is a main feature in the HF heating of the ionosphere. The numerical simulations and experiments using HAARP facility have yielded a good understanding of the plasma processes in the ionosphere that lead to wave generation. In the high-latitude ionosphere these waves are excited under most conditions, with and without an auroral electrojet or modulated heating. The studies using both numerical simulations and experiments under these different conditions are presented in this chapter. The essential mechanism is a multistep process in which the pressure gradient in the heated region in the F region drives a local diamagnetic current, which excites magnetosonic waves propagating across the magnetic field, which in turn excites shear Alfvén waves in the E region. The dominance of the Hall conductivity over the Pederson conductivity due to the strong coupling of the ion and neutral dynamics is responsible for the conversion of the compressional to shear modes. The shear Alfvén waves propagating along the field lines, to the ground and to the magnetosphere, were detected by ground- and satellite-based measurements.

In the mid-latitude ionosphere where there is no steady current or electrojet, the same mechanism is effective. In this region the simulations take into account the curved geometry of the Earth's dipole field and yield some new features in the generation of EMIC waves in the magnetosphere. In the equatorial ionosphere where the equatorial electrojet is prevalent, HF heating is expected to generate

low-frequency waves by the same mechanism as in the high and mid latitudes. A striking feature of the equatorial ionosphere is its highly enhanced Cowling conductivity, which can lead to more efficient wave generation.

Observations by ground radars (see chapter 1 of this volume) and low Earth orbit satellites (see chapter 2 of this volume) show that low-frequency waves are critical to a number of processes occurring in the ionosphere and magnetosphere. The numerical simulations presented here are an attempt to stimulate investigations to further our understanding of these processes.

### ACKNOWLEDGMENT

The research at the University of Maryland is supported by NSF grant AGS-1158206 and ONR/MURI grant FA95501410019. B.E. acknowledges the UK Engineering and Physical Sciences Research Council (EPSRC) for supporting this work under grant EP/M009386/1.

### REFERENCES

- Barr, R., and P. Stubbe (1991), ELF radiation from Tromsø “super heater” facility, *Geophys. Res. Lett.*, *18*, 1035, doi:10.1029/91GL01156.
- Bernhardt, P. A., C. A. Tepley, and L. M. Duncan (1989), Airglow enhancements associated with plasma cavities formed during ionospheric heating experiments, *J. Geophys. Res.*, *94*(A7), 9071–9092.
- Blagoveshchenskaya, N., T. Borisova, T. Yeoman, and M. Rietveld (2011), The effects of modifications of a high-latitude ionosphere by high-power HF radio waves, Part 1. *Radiophys. Quantum Elect.*, *53*(9/10), 512–531.
- Cohen, M. B., and M. Gołkowski (2013), 100 days of ELF/VLF generation via HF heating with HAARP, *J. Geophys. Res.*, *118*(A10), 6597–6607.
- Eliasson, B. (2010), Numerical simulations of the Fourier transformed Vlasov–Maxwell system in higher dimensions—Theory and applications. *Trans. Theor. Stat. Phys.*, *39*(5), 387–465, doi:10.1080/00411450.2011.563711.
- Eliasson, B., and K. Papadopoulos (2008), Numerical study of mode conversion between lower hybrid and whistler waves on short-scale density striations, *J. Geophys. Res.*, *113*(A9), A10301, doi:10.1029/2008JA013261.
- Eliasson, B., and K. Papadopoulos (2009), Penetration of ELF currents and magnetic fields into the Earth's equatorial ionosphere, *J. Geophys. Res.*, *114*, A10301.
- Eliasson, B., X. Shao, G. Milikh, E. Mishin, and K. Papadopoulos (2012), Numerical modeling of artificial ionospheric layers driven by high-power HF heating. *J. Geophys. Res.*, *117*, A10321, doi:10.1029/2012JA018105.
- Eliasson, B., C.-L. Chang, and K. Papadopoulos (2012), Generation of ELF and ULF electromagnetic waves by modulated heating of the ionospheric F2 region, *J. Geophys. Res.*, *117*, doi:10.1029/2012JA017935

- Ganguly, S., W. Gordon, and K. Papadopoulos (1986), Active nonlinear ultralow-frequency generation in the ionosphere, *Phys. Rev. Lett.*, *57*, 641–644, doi:10.1103/PhysRevLett.57.641.
- Greifinger, C. (1972), Ionospheric propagation of oblique hydromagnetic plane waves at micropulsation frequencies, *J. Geophys. Res.*, *77* (13), 2377–2391.
- Gurevich, A. (2007), Nonlinear effects in the ionosphere, *Physics—Uspekhi*, *50*, 1091, doi:10.1070/PU2007v050n11ABEH006212.
- Guzdar, P. N., N. A. Gondarenko, K. Papadopoulos, G. M. Milikh, A. S. Sharma, P. Rodriguez, Yu. V. Tokarev, Yu. I. Belov, and S. L. Ossakow (2000), Diffraction model of ionospheric irregularity-induced heater-wave pattern detected on the WIND satellite, *Geophys. Res. Lett.*, *27*(3), 317–320.
- Jain, N., B. Eliasson, A. S. Sharma, and K. Papadopoulos (2012), Penetration of ELF currents and electromagnetic fields into the off-equatorial E-region of the Earth's ionosphere, arXiv:1201.5349v1 [physics.plasm-ph].
- Helliwell, R. A., J. P. Katsufurakis, and M. L. Trimpi (1973) Whistler-induced amplitude perturbations in VLF propagation, *J. Geophys. Res.*, *78*, 4679–4688.
- Hughes, W. J. (1983), Hydromagnetic waves in the magnetosphere, *Rev. Geophys. Space Phys. (US Nat. rep. to IUGG, 1979–1982)*, *21*, 508–520.
- Kotik D. S., A. V. Ryabov, E. N. Ermakova, A. V. Pershin, V. N. Ivanov, and V. P. Esin (2013), Properties of ULF / VLF signals generated by SURA facility in the upper ionosphere, *Radiophys. and Quant. Electr.*, *56*(6), 344–354.
- Leyser, T. B. (2001), Stimulated electromagnetic emissions by high-frequency electromagnetic pumping of the ionospheric plasma, *Space Sci. Rev.*, *98*, 223–328.
- Lysak, R. L. (1997), Propagation of Alfvén waves through the ionosphere, *Phys. Chem. Earth*, *22*, 757–766.
- Milikh, G. M., and K. Papadopoulos (2007), Enhanced ionospheric ELF/VLF generation efficiency by multiple timescale modulated heating, *Geophys. Res. Lett.*, *34*, L20804.
- Mishin, E.V., W.J. Burke, and T. Pedersen (2004), On the onset of HF-induced airglow at magnetic zenith, *J. Geophys. Res.*, *109*, A02305, doi:10.1029/2003JA010205
- Moore, R. C. (2007), ELF/VLF wave generation by modulated heating of the auroral electrojet, PhD thesis, Stanford Univ.
- Najmi, A., Eliasson, B., Shao, X., Milikh, G., Sharma, A. S., Papadopoulos, K. (2016), Theoretical studies of fast stochastic electron heating near the upper hybrid layer, *Radio Sci.* (submitted).
- Papadopoulos, K., A. S. Sharma, and C. L. Chang (1989), On the efficient operation of a plasma ELF antenna driven by modulation of ionospheric currents, *Comm. Plasma Phys. and Cont. Fus.*, *13*, 1–17.
- Papadopoulos, K., C. L. Chang, P. Vitello, and A. Drobot (1990), On the efficiency of ionospheric ELF generation, *Radio Sci.*, *25*(6), 1311–1320, doi:10.1029/RS025i006p01311.
- Papadopoulos, K., H.-B. Zhou and A.S. Sharma (1994), The role of helicon waves magnetospheric and ionospheric physics, *Comm. Plasma Phys. Cont. Fusion*, *15*(6), 321–337.
- Papadopoulos, K., T. Wallace, G. M. Milikh, W. Peter, and M. McKarrick (2005), The magnetic response of the ionosphere to pulsed HF heating, *Geophys. Res. Lett.*, *32*, L13101, doi:10.1029/2005GL023185
- Papadopoulos, K., N. Gumerov, X. Shao, C. L. Chang, and I. Doxas (2011a), HF driven currents in the ionosphere, *Geophys. Res. Lett.*, *38*, L12103, doi:10.1029/2011GL047368
- Papadopoulos, K., C.-L. Chang, J. Labenski, and T. Wallace (2011b), First demonstration of HF-driven ionospheric currents, *Geophys. Res. Lett.*, *38*, L20107, doi:10.1029/2011GL049263
- Payne, J. A., U. S. Inan, F. R. Foust, T. W. Chevalier, and T. F. Bell (2007), HF modulated ionospheric currents, *Geophys. Res. Lett.*, *34*, L23101, doi:10.1029/2007GL031724.
- Pedersen, T. R., and E. A. Gerken (2005), Creation of visible artificial optical emissions in the aurora by high-power radio waves, *Nature*, *433*, 498–500, doi:10.1038/nature03243
- Pedersen, T., B. Gustavsson, E. Mishin, E. MacKenzie, H. Carlson, M. Starks, and T. Mills (2009), Optical ring formation and ionization production in high-power HF heating experiments at HAARP, *Geophys. Res. Lett.*, *36*, L18107, doi:10.1029/2009GL040047
- Piddyachiy, D., U. S. Inan, T. F. Bell, N. G. Lehtinen, and M. Parrot (2008), DEMETER observations of an intense upgoing column of ELF/VLF radiation excited by the HAARP HF heater, *Geophys. Res. Lett.*, *37*, L02106, doi:10.1029/2009GL04189
- Pilipenko, V., E. Fedorov, K. Mursula, and T. Pikkarainen (2005), Generation of magnetic noise bursts during distant rocket launches, *Geophysica*, *41*(1/2), 57–72.
- Platino, M., U. S. Inan, T. F. Bell, M. Parrot, and E. J. Kennedy (2006), DEMETER observation of ELF waves injected with the HAARP HF transmitter, *Geophys. Res. Lett.*, *33*, L16101, doi:10.1029/2006GL026462
- Rietveld, M. T., R. Barr, H. Kopka, E. Nielson, P. Stubbe and R. L. Dowden (1984), Ionospheric heater beam scanning: A new technique for ELF studies of the auroral ionosphere, *Radio Sci.*, *19*(4), 1069–1077, doi:10.1029/RS019i004p01069
- Rietveld, M. T., H.-P. Maelshagen, P. Stubbe, H. Kopka, and E. Nielsen (1987a), The characteristics of ionospheric heating-produced ELF/VLF waves over 32 hours, *J. Geophys. Res.*, *92*, 8707, doi:10.1029/JA092iA08p08707
- Rietveld, M. T., P. Stubbe, and H. Kopka (1989), On the frequency dependence of ELF/VLF waves produced by modulated ionospheric heating, *Radio Sci.*, *24*(3), 270–278.
- Rietveld, M. T., M. J. Kosch, N. F. Blagoveshchenskaya, V. A. Kornienko, T. B. Leyser, and T. K. Yeoman (2003), Ionospheric electron heating, optical emissions, and striations induced by powerful HF radio waves at high latitudes: Aspect angle dependence. *J. Geophys. Res.*, *108*(A4), doi: 10.1029/2002JA009543
- Shao, X., B. Eliasson, A.S. Sharma, G. Milikh, and K. Papadopoulos (2012), Attenuation of whistler waves through conversion to lower hybrid waves in the low-altitude ionosphere, *J. Geophys. Res.*, *117*, 2011JA017339.
- Sharma, A. S., B. Eliasson, X. Shao, and K. Papadopoulos (2016), Excitation of low frequency waves in HF heating in the mid-latitude ionosphere, *Radio Sci.* (submitted).
- Stubbe, P., H. Kopka, and R. L. Dowden (1981), Generation of ELF and VLF Waves by polar electrojet modulation: Experimental results, *J. Geophys. Res.*, *86*, 9073–9078.

- Stubbe, P. (1996), Review of ionospheric modification experiments at Tromsø, *J. Atmos. Terr. Phys.*, 58, 349–368.
- Surkov, V., E. Fedorov, V. Pilipenko, and K. Yumoto (1997), Ionospheric propagation of MHD disturbances from the equatorial electrojet, *Geomagn. Aeronomy.*, 37, 61–70.
- Vartanyan, A., G. M. Milikh, B. Eliasson, A. C. Najmi, C. L. Chang, M. Parrot, and K. Papadopoulos (2016), Generation of whistler waves by continuous HF heating of the upper ionosphere. *Radio Sci.* (submitted).
- Utlaut, W. F., E. J. Viollette, and L. L. Melanson (1974), Radar cross section measurements and vertical incidence effects observed with Platteville at reduced power, *Radio Sci.*, 9(11), 1033–1040, doi:10.1029/RS009i011p01033.
- Zhou, H.B., K. Papadopoulos, A.S. Sharma, and C.-L. Chang (1996), Electron-magnetohydrodynamic response of a plasma to an external current pulse, *Phys. Plasmas*, 3, 1484–1494.